JOURNAL OF PROPULSION AND POWER
Vol. 25, No. 1, January–February 2009

Reduced-Order Model for Combustion Instability in a Two-Dimensional Duct with a Flameholder

Sarma L. Rani*
CFD Research Corporation, Huntsville, Alabama 35805

DOI: 10.2514/1.35958

A reduced-order model for combustion instability in a two-dimensional duct with a flameholder is presented. A linear flame-response function for a premixed flame of arbitrary mean shape is derived using the *G*-equation approach. Perturbations consisting of coupled axial and transverse modes are superimposed on system mean flow conditions and analyzed for instability. Test cases involving variations of duct geometry, flameholder location, and mean flame shape are considered for evaluating the reduced-order model. Mean flow and temperature conditions and mean heat-release rate, needed as inputs to the model, are obtained from highly resolved two-dimensional large-eddy simulation data for the same geometry. The pressure power spectrum from large-eddy simulation is available for two cases: 1) with the flameholder located symmetrically between the top and bottom walls of the duct and 2) with the flameholder offset vertically by a small distance relative to the duct height. For the first case, the large-eddy simulation pressure power spectrum shows a dominant transverse instability mode that is also captured by the model. In the second case, large-eddy simulation shows that a small vertical offset damps the dominant transverse mode found in the zero-offset first case. The model also qualitatively supports this trend. For additional test cases in which large-eddy simulation data are not available, the model is seen to produce qualitatively consistent trends.

Nomenclature

$A_n^{\pm}$	=	amplitudes of the waves propagating in the positive and negative x directions
a	=	vertical distance between the flameholder and the upper wall.
$\bar{c}$	=	mean sound speed
D	=	height of the duct
dA	=	area of the flame-surface element
f	=	functional form of the flame surface
h_r	=	heat of reaction
$k_n^{\pm}$	=	axial wave numbers of the nth mode propagating in the positive and negative x directions
L_f	=	length of the flame along the streamwise (axial) direction
$\bar{M}$	=	mean flow Mach number ($\bar{u}/\bar{c}$)
p'	=	pressure fluctuation
Q	=	ensemble-averaged heat-release rate
$\tilde{Q}$	=	instantaneous heat-release rate
q	=	ensemble-averaged heat-release rate per unit surface area of the flame ($\bar{q} + q'$)
$\bar{q}$	=	time-mean heat-release rate per unit surface area of the flame
q'	=	time-fluctuating heat-release rate per unit surface area of the flame
s_L	=	laminar burning velocity
s_T	=	turbulent burning velocity
u, v	=	ensemble-averaged velocity components along the x and y directions
$\bar{u}$	=	mean flow speed in the streamwise direction
u', v'	=	streamwise and transverse fluctuating velocities
u_n'	=	velocity fluctuation normal to the mean flame surface
Z_{inlet}	=	inlet impedance of the duct
γ	=	ratio of specific heats
$\bar{\rho}$	=	mean density
ϕ	=	equivalence ratio
Ω	=	complex frequency
$\hat{\cdot}$	=	Fourier transform in frequency space
$\bar{\cdot}$	=	time-mean value of a quantity
$\cdot'$	=	fluctuation from the time mean
$\tilde{\cdot}$	=	instantaneous value of a quantity

Presented as Paper 5649 at the 43rd AIAA/ASME/SAE/ASEE Joint Propulsion Conference, Cincinnati, OH, 8–11 July 2007; received 30 November 2007; revision received 25 April 2008; accepted for publication 31 May 2008.

*215 Wynn Drive; rln_sarma@yahoo.com.

I. Introduction

FLAME and combustion instabilities have been an important concern in the design and operation of combustors and augmenters for a number of decades. Flame instability is associated with combustor/augmenter operating conditions under which a flame cannot be sustained and blowout occurs. Current physical understanding of the blowout of bluff-body-stabilized flames owes a lot to the pioneering work of a number of researchers about half a century ago [1–6]. Recently, Soteriou and Mehta [7] investigated the relationship between flame vorticity dynamics and lean blowout of a bluff-body-stabilized flame.

Combustion instability refers to self-excited acoustic (pressure) oscillations generated by the feedback coupling between the natural acoustic modes of the system and an oscillatory combustion process such as heat-release oscillations [8–10]. The process of thermo-acoustic coupling between the system pressure oscillations and flame heat-release oscillations is illustrated schematically in Fig. 1.

Both flame and combustion instabilities may greatly affect augmenter operability and may lead to severe restrictions in the operating envelope of the augmenter. Consequently, there is considerable interest in identifying mechanisms that drive these instabilities and the conditions under which instabilities occur and in developing practical approaches for their control. In this study, we concern ourselves with only combustion instabilities.

Experimental and/or computational fluid dynamics (CFD) parametric studies to map the stability boundaries of augmenters are cost-prohibitive. Hence, efficient reduced-order analysis tools capable of characterizing system instabilities have an important role to play. Linear/nonlinear stability analysis is one such analytical modeling tool. Linear stability analysis predicts the amplitude growth rate of an acoustic mode in the limit of small perturbations. The amplitude growth rate provides insight into the stability of a given mode, but cannot be used to determine if any of the linearly

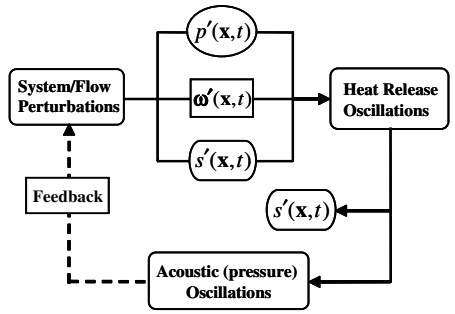

Fig. 1 Feedback coupling between pressure and heat-release oscillations leading to combustion instability; $p'(\mathbf{x},t)$, $\omega'(\mathbf{x},t)$, and $s'(\mathbf{x},t)$ are fluctuations in pressure, vorticity vector, and entropy, respectively.

unstable modes will reach a limit cycle that exceeds the design specifications of the system. Nonlinear stability analysis can provide information on limit-cycle amplitudes and can predict the system response to nonlinear triggering events encountered, for example, in rockets.

A number of researchers have studied reduced-order modeling of combustion instabilities, particularly in 1-D geometries and less so in 2-D and 3-D geometries. Even in studies in which 2-D and 3-D geometries are considered, coupling of nonaxial and axial modes (e.g., coupling of radial, azimuthal, and axial modes in a cylindrical combustor) is typically ignored because of the analytical complexity it introduces. Most existing studies on combustion instability are linear in nature. A comprehensive review of linear stability analysis of gas turbine combustors was provided in reference [11].

Three-dimensional thermoacoustic oscillations in a premix combustor were modeled by Akamatsu and Dowling [12], and the coupling between various modes was also included. Heat release was considered to occur in a single plane at the exit of a premixing duct, whereas heat-release oscillations were modeled simply as a function of flow velocity perturbations at the fuel nozzle position. The former assumption is strictly valid in the limit of low excitation Strouhal numbers: that is, $St = \Omega_{\text{real}} L_f / U_o \ll 1$, where Ω_{real} is the real part of the complex frequency Ω, L_f is a typical length scale of the flame, and U_o is a characteristic velocity scale. This assumption is rather restrictive in the context of bluff-body-stabilized flames (see Fig. 2), as our large-eddy simulation (LES) results will show.

Hubbard and Dowling [13,14] studied thermoacoustic instabilities in an industrial gas turbine system. In that study, they considered fluctuations in equivalence ratio at the flame as a function of velocity fluctuations in the fuel injector that have convected downstream to the flame location. Along similar lines, Dowling and Hubbard [15], Stow and Dowling [16], and Armitage et al. [17] have all studied thermoacoustic oscillations in lean premixed combustors with varying complexities in linear stability modeling, flame-response function, and geometry. Work by other researchers on 3-D linear stability analysis of a gas turbine combustor includes that of Fleifil et al. [18], Wee et al. [19], and that of You et al. [20]. There has also been a significant amount of research on nonlinear stability analysis by Culick [21–23], Bumley and Culick [24], Margolis [25–27], and Flandro et al. [28].

In spite of the extensive research on the topic of combustion instabilities, it seems that an analytical study of a 2-D or a 3-D flameholder configuration (see Fig. 2), which is of interest in an augmenter, does not exist. An important modeling aspect of the current work is to derive a flame-response function for a flame of arbitrary quiescent shape. Existing studies of the flame-response functions by Lieuwen [29], Lieuwen and Neumeier [30], Preetham and Lieuwen [31,32], Dowling [33], and Kopitz et al. [34] assume either simplified mean flame shapes (e.g., linear function of radial direction) or that heat release occurs in a plane. Hence, flame-response models are needed that are applicable to arbitrary mean flame shapes, especially in bluff-body-stabilized-flame applications. In view of the preceding discussion, there is a need to investigate the effects of realistic flame shapes and their response functions as well as of coupled 2-D and 3-D perturbations to get a more accurate picture of combustion instability.

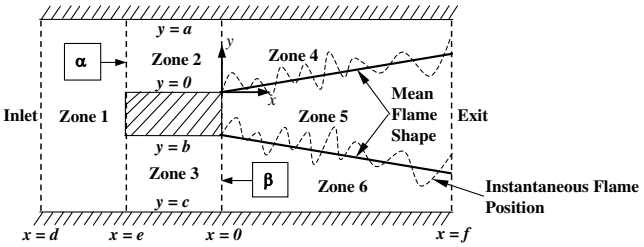

Fig. 2 Geometry and zonal network for the linear stability analysis of a 2-D bluff-body-stabilized flame.

In the zonal-based reduced-order-modeling approach followed in this study, some of the preceding modeling issues have been addressed. The model predicts the stability of the mean system conditions to coherent perturbations of small amplitude compared with the mean conditions. First, we consider 2-D coupled axial and transverse perturbations superimposed on mean conditions and investigate their temporal evolution using linear stability analysis. Further, we have developed a flame-response model that relates fluctuations in heat-release rate to those in the flame-surface area for a premixed flame of arbitrary mean shape. Mean system properties such as the mean velocity field, temperature, and flame shape, which are inputs to the model, are obtained from a priori 2-D LES data. Model results will be validated against the highly resolved 2-D LES data.

Next, we present a detailed derivation of the stability analysis model, as well as of the flame-response function. The extensive discussion of the modeling approach will also serve as a useful tutorial. Subsequently, results from a number of test cases are presented. Direct comparison with 2-D LES data are, however, available only for two cases. For the other cases, qualitative trends from model predictions are discussed.

II. Reduced-Order Model

To derive the reduced-order model, we begin with the inhomogeneous linear acoustic-wave equation given by

$$\frac{1}{\bar{c}^2}\frac{\bar{\mathrm{D}}^2 p'}{\bar{\mathrm{D}}t^2} - \nabla^2 p' = \frac{\gamma - 1}{\bar{c}^2}\frac{\bar{\mathrm{D}} q_v'}{\bar{\mathrm{D}}t} \tag{1}$$

where

$$\frac{\bar{\mathrm{D}}}{\bar{\mathrm{D}}t} = \frac{\partial}{\partial t} + \bar{\mathbf{u}} \bullet \nabla$$

$\bar{\mathbf{u}}$ is the mean velocity vector; p' and q_v' are the fluctuating components of pressure and heat-release rate per unit volume, respectively; $\bar{c}$ is the mean sound speed; and γ is the ratio of specific heats.

Assuming that the mean flow is in the axial (x) direction, $\bar{\mathbf{u}} = \bar{u}\,\hat{\mathbf{i}}$, and considering regions with no unsteady heat release, the wave equation in its 2-D Cartesian form is given by

$$\frac{1}{\bar{c}^2}\frac{\partial^2 p'}{\partial t^2} + 2\frac{\bar{M}}{\bar{c}}\frac{\partial^2 p'}{\partial t \partial x} + (\bar{M}^2 - 1)\frac{\partial^2 p'}{\partial x^2} - \frac{\partial^2 p'}{\partial y^2} = 0 \tag{2}$$

where y is the transverse direction and $\bar{M} = \bar{u}/\bar{c}$ is the mean flow Mach number.

Next, we derive the fluctuation forms of pressure, density, velocity components, and vorticity. We begin in Secs. II.A–II.C by deriving the respective fluctuation forms for a generic domain. Subsequently, in Secs. II.D and II.E, we modify the generic fluctuation forms to account for the specific domain of interest shown in Fig. 2.

A. Generic Form of Pressure and Density Fluctuations

Assuming an impermeability boundary condition along the transverse (y) direction, we can solve Eq. (2) by applying $\partial p'/\partial y = 0$ at the two transverse boundaries (located at, say, $y = \pm L$). In Secs. II.A–II.C, for convenience, we consider a coordinate system with $y = 0$ located midway between the two transverse boundaries. However, the coordinate system used in the actual domain of interest is indicated in Fig. 2 and is different from that in the current discussion.

Using the impermeability boundary condition at $y = \pm L$ and assuming harmonic temporal dependence of pressure fluctuations, we can solve Eq. (2) for the complete form of $p'(x, y, t)$:

$$p'(x, y, t) = e^{i\Omega t} \sum_{n=1}^{\infty} (A_n^+ e^{ik_n^+ x} + A_n^- e^{ik_n^- x}) \cos\left(\frac{n\pi}{L} y\right) \tag{3}$$

where A_n^+ and A_n^- are the amplitudes of waves propagating in the positive and negative x directions, respectively. The wave numbers in the positive and negative x directions, k_n^+ and k_n^-, are

$$k_n^{\pm} = \frac{\frac{\Omega \bar{M}}{\bar{c}} \mp \left[\frac{\Omega^2}{\bar{c}^2} - (1 - \bar{M}^2)\left(\frac{n\pi}{L}\right)^2\right]^{1/2}}{(1 - \bar{M}^2)} \tag{4}$$

Density fluctuations resulting from the preceding pressure fluctuations can be written as

$$\begin{aligned} \rho'(x, y, t) &= \frac{p'(x, y, t)}{\bar{c}^2} \\ &= \frac{1}{\bar{c}^2} e^{i\Omega t} \sum_{n=1}^{\infty} (A_n^+ e^{ik_n^+ x} + A_n^- e^{ik_n^- x}) \cos\left(\frac{n\pi}{L} y\right) \end{aligned} \tag{5}$$

B. Generic Form of Velocity Fluctuations

Axial velocity fluctuations $u'(x, y, t)$ can be obtained from the linearized u'-momentum equation:

$$\bar{\rho} \frac{\partial u'}{\partial t} + \bar{\rho}\, \bar{u} \frac{\partial u'}{\partial x} = -\frac{\partial p'}{\partial x} \tag{6}$$

Because we already know $p'(x, y, t)$, we can readily obtain $u'(x, y, t)$ from the preceding equation, which given by

$$\begin{aligned} u'(x, y, t) = -\frac{1}{\bar{\rho}} e^{i\Omega t} \sum_{n=1}^{\infty} \Bigg(& \frac{k_n^+}{\Omega + \bar{u} k_n^+} A_n^+ e^{ik_n^+ x} \\ & + \frac{k_n^-}{\Omega + \bar{u} k_n^-} A_n^- e^{ik_n^- x} \Bigg) \cos\left(\frac{n\pi}{L} y\right) \end{aligned} \tag{7}$$

The transverse velocity fluctuations $v'(x, y, t)$ can be obtained from the v'-momentum equation, given by

$$\bar{\rho} \frac{\partial v'}{\partial t} + \bar{\rho}\, \bar{u} \frac{\partial v'}{\partial x} = -\frac{\partial p'}{\partial y} \tag{8}$$

From the preceding equation, we get

$$\begin{aligned} v'(x, y, t) = \frac{1}{\bar{\rho}} e^{i\Omega t} \sum_{n=1}^{\infty} \Bigg(& \frac{1}{\Omega + \bar{u} k_n^+} A_n^+ e^{ik_n^+ x} \\ & + \frac{1}{\Omega + \bar{u} k_n^-} A_n^- e^{ik_n^- x} \Bigg) \frac{n\pi}{L} \sin\left(\frac{n\pi}{L} y\right) \end{aligned} \tag{9}$$

A useful attribute of the $\cos(n\pi y/L)$ function is its orthonormality property, as defined next:

$$\begin{aligned} \frac{1}{L} \int_{-L}^{L} \cos\left[\frac{m\pi}{L} y\right] \cos\left[\frac{n\pi}{L} y\right] &= \delta_{mn} \\ \int_{-L}^{L} \sin\left[\frac{m\pi}{L} y\right] \cos\left[\frac{n\pi}{L} y\right] &= 0 \end{aligned} \tag{10}$$

This property is used extensively for analytical simplification in the analysis that follows.

C. Generic Form of Vorticity Fluctuations

In the current formulation, it is necessary to consider vorticity fluctuations, as they play an important role in distorting the flame, leading to flame-surface-area fluctuations. Vorticity fluctuations convect with the mean flow (i.e., convect downstream) in the current study. They can be represented as

$$\begin{aligned} u'_\omega(x, y, t) &= e^{i\Omega t} \sum_{n=1}^{\infty} \hat{V}_n e^{-i\Omega x/\bar{u}} \cos\left(\frac{n\pi}{L} y\right) \\ v'_\omega(x, y, t) &= \frac{i\Omega}{\bar{u}} e^{i\Omega t} \sum_{n=1}^{\infty} \hat{V}_n e^{-i\Omega x/\bar{u}} \frac{L}{n\pi} \sin\left(\frac{n\pi}{L} y\right) \end{aligned} \tag{11}$$

In the current analysis, we ignore entropy fluctuation effects.

D. Unknown Coefficients

So far, we have derived the generic fluctuation forms of pressure, density, vorticity, and the two components of velocity. These fluctuation forms are valid in regions without unsteady heat release. The unknown terms in these fluctuations are the coefficients $A_n^{\pm}$ and $\hat{V}_n$ ($n = 1, 2, \ldots$). We therefore need to determine the equations that can be solved for these unknown coefficients. Because we have already used the impermeability boundary condition in deriving the fluctuation forms, we have at our disposal the inlet and outlet boundary conditions and the various matching conditions at the zonal interfaces.

The geometry of interest, the coordinate system, and the zonal configuration are indicated in Fig. 2. The flow domain is divided into six zones: zone 1 is the inlet region of the duct; zones 2 and 3 are the flow above and below the flameholder; zones 4 and 6 are upstream of the flame; and zone 5 is downstream of the flame, containing combustion products as well as unburned reactants. The mean flame shape and the instantaneous flame shape due to the superimposed perturbations are indicated in Fig. 2. It is assumed that the flame is a thin sheet separating the cold reactants and the hot products and that the heat release occurs only at the flame surface. For the flow conditions of interest (see Table 1), the thin-flame assumption is reasonable [35], as the ratio of the characteristic eddy size to the laminar flame thickness of propane gas is $\mathcal{O}(10^2)$ and the ratio of the turbulent rms velocity to the laminar flame speed is $\mathcal{O}(10)$. We also assume that the flame base remains anchored to the bluff body, as shown in Fig. 2.

E. Fluctuations Forms in Zones 1–6

From Fig. 2, it is clear that there is no unsteady heat release in any of the six zones into which the domain is divided. Hence, the pressure, density, velocity, and vorticity-fluctuation expressions derived in Secs. II.A–II.C are valid in zones 1–6, except for zone 5, which is not bounded by walls in the y direction. However, these fluctuation expressions have to be adjusted to account for the coordinate system indicated in Fig. 2. Fluctuation forms in zone 5 are derived using the impermeability boundary condition at $x = 0$. We now present the individual zonal forms of the pressure, density, and velocity fluctuations.

Table 1 Flow conditions and geometry for the two LES runs

Mean streamwise flow velocity $\bar{u}$	50 m/s
Mean pressure $\bar{p}$	1.0 atm
Mean incoming speed of sound $\bar{c}$	345 m/s
Mean incoming temperature $\bar{T}$	300 K
Mean temperature of burned gases $\bar{T}_b$	2300 K
Mean incoming Mach number $\bar{M}$	0.15
Incoming turbulence intensity	5%
Bluff-body height	0.5 in.
Bluff-body length	1.0 in.
Total duct height	3.0 in.
Duct length downstream of the bluff body	5.55 in.
Incoming equivalence ratio ϕ	1.0

1. Zone 1

An important aspect in obtaining the appropriate zonal fluctuation expressions is that in addition to the impermeability boundary condition at $y = a$ and c in zone 1, we use the orthonormality property of the cosine function between the two walls (at $y = a$ and c). To use orthonormality of the cosine function between $y = a$ and c, the generic form $\cos((n\pi/L)y)$ is modified for zone 1 as

$$\cos\left[\frac{n\pi}{L_{\text{zone 1}}}Y_{\text{zone 1}}\right] = \cos\left[\frac{n\pi}{(\frac{a-c}{2})}\left(y - \frac{a+c}{2}\right)\right]$$

where $Y_{\text{zone 1}}$ is the local transverse coordinate with $Y_{\text{zone 1}} = 0$ at $y = (a + c)/2$. As a result, the orthonomality property is now expressed as

$$\frac{1}{(\frac{a-c}{2})}\int_c^a \mathrm{d}y \cos\left[\frac{m\pi}{(\frac{a-c}{2})}\left(y - \frac{a+c}{2}\right)\right] \times \cos\left[\frac{n\pi}{(\frac{a-c}{2})}\left(y - \frac{a+c}{2}\right)\right] = \delta_{mn} \tag{12}$$

where $(a - c)/2$ is half of the y distance between the two walls at $y = a$ and c. We now arrive at the following fluctuation expressions in zone 1:

$$\begin{aligned}
p'_1(x,y,t) &= e^{i\Omega t}\sum_{n=1}^{\infty}(A_n^+ e^{ik_n^+ x} + A_n^- e^{ik_n^- x})\cos\left[\frac{n\pi}{(\frac{a-c}{2})}\left(y - \frac{a+c}{2}\right)\right]\\
\rho'_1(x,y,t) &= \frac{1}{\bar{c}^2}e^{i\Omega t}\sum_{n=1}^{\infty}(A_n^+ e^{ik_n^+ x} + A_n^- e^{ik_n^- x})\cos\left[\frac{n\pi}{(\frac{a-c}{2})}\left(y - \frac{a+c}{2}\right)\right]\\
u'_1(x,y,t) &= -\frac{1}{\bar{\rho}}e^{i\Omega t}\sum_{n=1}^{\infty}\left(\frac{k_n^+}{\Omega + \bar{u}k_n^+}A_n^+ e^{ik_n^+ x} + \frac{k_n^-}{\Omega + \bar{u}k_n^-}A_n^- e^{ik_n^- x}\right)\cos\left[\frac{n\pi}{(\frac{a-c}{2})}\left(y - \frac{a+c}{2}\right)\right]\\
v'_1(x,y,t) &= \frac{1}{\bar{\rho}}e^{i\Omega t}\sum_{n=1}^{\infty}\left(\frac{1}{\Omega + \bar{u}k_n^+}A_n^+ e^{ik_n^+ x} + \frac{1}{\Omega + \bar{u}k_n^-}A_n^- e^{ik_n^- x}\right)\frac{n\pi}{(\frac{a-c}{2})}\sin\left[\frac{n\pi}{(\frac{a-c}{2})}\left(y - \frac{a+c}{2}\right)\right]
\end{aligned} \tag{13}$$

2. Zones 2 and 4

In zones 2 and 4, the total velocity fluctuations are a combination of both acoustic- and vorticity-induced velocity fluctuations and we use orthonormality between $y = 0$ and a. This gives rise to the following equations:

$$\begin{aligned}
p'_{2,4}(x,y,t) &= e^{i\Omega t}\sum_{n=1}^{\infty}(A_n^+ e^{ik_n^+ x} + A_n^- e^{ik_n^- x})\cos\left[\frac{n\pi}{(\frac{a}{2})}\left(y - \frac{a}{2}\right)\right]\\
\rho'_{2,4}(x,y,t) &= \frac{1}{\bar{c}^2}e^{i\Omega t}\sum_{n=1}^{\infty}(A_n^+ e^{ik_n^+ x} + A_n^- e^{ik_n^- x})\cos\left[\frac{n\pi}{(\frac{a}{2})}\left(y - \frac{a}{2}\right)\right]\\
u'_{2,4}(x,y,t) &= -\frac{1}{\bar{\rho}}e^{i\Omega t}\sum_{n=1}^{\infty}\left(\frac{k_n^+}{\Omega + \bar{u}k_n^+}A_n^+ e^{ik_n^+ x} + \frac{k_n^-}{\Omega + \bar{u}k_n^-}A_n^- e^{ik_n^- x}\right)\times\cos\left[\frac{n\pi}{(\frac{a}{2})}\left(y - \frac{a}{2}\right)\right] + e^{i\Omega t}\sum_{n=1}^{\infty}\hat{V}_n e^{-i\Omega x/\bar{u}}\cos\left[\frac{n\pi}{(\frac{a}{2})}\left(y - \frac{a}{2}\right)\right]\\
v'_{2,4}(x,y,t) &= \frac{1}{\bar{\rho}}e^{i\Omega t}\sum_{n=1}^{\infty}\left(\frac{1}{\Omega + \bar{u}k_n^+}A_n^+ e^{ik_n^+ x} + \frac{1}{\Omega + \bar{u}k_n^-}A_n^- e^{ik_n^- x}\right)\frac{n\pi}{(\frac{a}{2})}\sin\left[\frac{n\pi}{(\frac{a}{2})}\left(y - \frac{a}{2}\right)\right]\\
&\quad + \frac{i\Omega}{\bar{u}}e^{i\Omega t}\sum_{n=1}^{\infty}\hat{V}_n e^{-i\Omega x/\bar{u}}\frac{(\frac{a}{2})}{n\pi}\sin\left[\frac{n\pi}{(\frac{a}{2})}\left(y - \frac{a}{2}\right)\right]
\end{aligned} \tag{14}$$

3. Zones 3 and 6

Vorticity-fluctuation contributions to the total velocity fluctuations are included in zones 3 and 6 as well, giving rise to the following expressions:

$$\begin{aligned}
p'_{3,6}(x,y,t) &= e^{i\Omega t}\sum_{n=1}^{\infty}(A_n^+ e^{ik_n^+ x} + A_n^- e^{ik_n^- x})\cos\left[\frac{n\pi}{(\frac{b-c}{2})}\left(y - \frac{b+c}{2}\right)\right]\\
\rho'_{3,6}(x,y,t) &= \frac{1}{\bar{c}^2}e^{i\Omega t}\sum_{n=1}^{\infty}(A_n^+ e^{ik_n^+ x} + A_n^- e^{ik_n^- x})\cos\left[\frac{n\pi}{(\frac{b-c}{2})}\left(y - \frac{b+c}{2}\right)\right]\\
u'_{3,6}(x,y,t) &= -\frac{1}{\bar{\rho}}e^{i\Omega t}\sum_{n=1}^{\infty}\left(\frac{k_n^+}{\Omega + \bar{u}k_n^+}A_n^+ e^{ik_n^+ x} + \frac{k_n^-}{\Omega + \bar{u}k_n^-}A_n^- e^{ik_n^- x}\right)\cos\left[\frac{n\pi}{(\frac{b-c}{2})}\left(y - \frac{b+c}{2}\right)\right] + e^{i\Omega t}\sum_{n=1}^{\infty}\hat{V}_n e^{-i\Omega x/\bar{u}}\cos\left[\frac{n\pi}{(\frac{b-c}{2})}\left(y - \frac{b+c}{2}\right)\right]\\
v'_{3,6}(x,y,t) &= \frac{1}{\bar{\rho}}e^{i\Omega t}\sum_{n=1}^{\infty}\left(\frac{1}{\Omega + \bar{u}k_n^+}A_n^+ e^{ik_n^+ x} + \frac{1}{\Omega + \bar{u}k_n^-}A_n^- e^{ik_n^- x}\right)\frac{n\pi}{(\frac{b-c}{2})}\sin\left[\frac{n\pi}{(\frac{b-c}{2})}\left(y - \frac{b+c}{2}\right)\right]\\
&\quad + \frac{i\Omega}{\bar{u}}e^{i\Omega t}\sum_{n=1}^{\infty}\hat{V}_n e^{-i\Omega x/\bar{u}}\frac{(\frac{b-c}{2})}{n\pi}\sin\left[\frac{n\pi}{(\frac{b-c}{2})}\left(y - \frac{b+c}{2}\right)\right]
\end{aligned} \tag{15}$$

4. Zone 5

As discussed earlier, fluctuation forms in zone 5 differ from those in other zones, as they are not bound by walls in the y direction in zone 5. In deriving the fluctuation forms in zone 5, we begin with the following generic form (vorticity contributions are ignored in this zone downstream of the flame):

$$\begin{aligned}
p'_5(x,y,t) &= e^{i\Omega t}\sum_{n=1}^{\infty}(A_n^+ e^{ik_n^+ x} + A_n^- e^{ik_n^- x})(B_n^+ e^{-ik_y y} + B_n^- e^{ik_y y}),\\
\rho'_5(x,y,t) &= \frac{1}{\bar{c}^2}e^{i\Omega t}\sum_{n=1}^{\infty}(A_n^+ e^{ik_n^+ x} + A_n^- e^{ik_n^- x})(B_n^+ e^{-ik_y y} + B_n^- e^{ik_y y}),\\
u'_5(x,y,t) &= -\frac{1}{\bar{\rho}}e^{i\Omega t}\sum_{n=1}^{\infty}\left(\frac{k_n^+}{\Omega + \bar{u}k_n^+}A_n^+ e^{ik_n^+ x} + \frac{k_n^-}{\Omega + \bar{u}k_n^-}A_n^- e^{ik_n^- x}\right)(B_n^+ e^{-ik_y y} + B_n^- e^{ik_y y}),\\
v'_5(x,y,t) &= \frac{1}{\bar{\rho}}e^{i\Omega t}\sum_{n=1}^{\infty}\left(\frac{1}{\Omega + \bar{u}k_n^+}A_n^+ e^{ik_n^+ x} + \frac{1}{\Omega + \bar{u}k_n^-}A_n^- e^{ik_n^- x}\right)(-ik_y B_n^+ e^{-ik_y y} + ik_y B_n^- e^{ik_y y})
\end{aligned} \tag{16}$$

In zone 5, impermeability boundary condition can be applied along the bluff-body wall at $x = 0$. This gives us

$$u'(x = 0, y, t) = 0 \Rightarrow \frac{k_n^+}{\Omega + \bar{u}k_n^+}A_n^+ + \frac{k_n^-}{\Omega + \bar{u}k_n^-}A_n^- = 0 \tag{17}$$

Using the preceding relationship between A_n^+ and A_n^-, we eliminate either A_n^+ or A_n^- from Eq. (16). After absorbing the remaining A_n^- or A_n^+ into $B_n^\pm$, we get the following forms of the perturbations in zone 5:

$$p'_5(x,y,t) = e^{i\Omega t}\sum_{n=1}^{\infty}\left(e^{ik_n^+ x} - \frac{\Omega+\bar{u}k_n^-}{\Omega+\bar{u}k_n^+}\frac{k_n^+}{k_n^-}e^{ik_n^- x}\right)(B_n^+ e^{-ik_y y} + B_n^- e^{ik_y y})$$

$$\rho'_5(x,y,t) = \frac{1}{\bar{c}^2}e^{i\Omega t}\sum_{n=1}^{\infty}\left(e^{ik_n^+ x} - \frac{\Omega+\bar{u}k_n^-}{\Omega+\bar{u}k_n^+}\frac{k_n^+}{k_n^-}e^{ik_n^- x}\right)(B_n^+ e^{-ik_y y} + B_n^- e^{ik_y y})$$

$$u'_5(x,y,t) = -\frac{1}{\bar{\rho}}e^{i\Omega t}\sum_{n=1}^{\infty}(e^{ik_n^+ x} - e^{ik_n^- x})(B_n^+ e^{-ik_y y} + B_n^- e^{ik_y y})$$

$$v'_5(x,y,t) = \frac{1}{\bar{\rho}}e^{i\Omega t}\sum_{n=1}^{\infty}\left(e^{ik_n^+ x} - \frac{1}{\Omega+\bar{u}k_n^-}\frac{k_n^+}{k_n^-}e^{ik_n^- x}\right) \times(-ik_y B_n^+ e^{-ik_y y} + ik_y B_n^- e^{ik_y y}) \tag{18}$$

Hence, the total list of unknown coefficients is (subscripts 1 through 6 in the next equation are the zone numbers) as follows:

For acoustic modes,

$$(A_n^{\pm})_{1,2,3,4,6}, (B_n^{\pm})_5 \tag{19a}$$

For vorticity modes,

$$(\hat{V}_n)_{2,3,4,6} \tag{19b}$$

which are obtained using zonal boundary and matching conditions. A detailed discussion of these conditions follows.

Again, we begin by deriving the generic zonal matching and boundary conditions in Sec. II.F, which are subsequently modified for the actual interfaces and inlet and exit boundaries in Secs. II.G and II.H.

F. Generic Zonal Matching and Boundary Conditions

We employ the zonal-interface matching conditions and the inlet and exit boundary conditions to derive the equations necessary to solve for the unknown coefficients indicated in Eq. (19). Deriving the matching conditions at the zonal interfaces involves integrating the fluctuating forms of the continuity, momentum-, and energy-balance equations in a differential volume of thickness dn normal to the interface of interest (d$n \to 0$). Next, we provide a generic discussion of the zonal matching process, and consider transverse (y) boundaries located at say $y = \pm L$.

1. *Linearized Continuity Equation*

The linearized fluctuating continuity equation is given by

$$\frac{\partial\rho'}{\partial t} + \nabla\bullet(\bar{\rho}\mathbf{u}' + \rho'\bar{\mathbf{u}}) = 0 \tag{20}$$

Multiplying Eq. (20) with $\cos(N\pi y/L)$ ($N > 0$ is an integer) and integrating over a differential volume dV of thickness dn normal to the interface, we get

$$\int_{dV}\mathrm{d}V\cos\left(\frac{N\pi}{L}y\right)\frac{\partial\rho'}{\partial t} + \int_{dV}\mathrm{d}V\cos\left(\frac{N\pi}{L}y\right)\nabla\bullet(\bar{\rho}\mathbf{u}'\rho'\bar{\mathbf{u}}) = 0 \tag{21}$$

where L is half the distance between the two y boundaries, located at say $y = \pm L$. The first term in the preceding equation reduces to zero as thickness d$n \to 0$. Using divergence theorem, the second term becomes a surface integral over the n^+ and n^- faces of the infinitesimal control volume. The other two control surfaces being along the walls will have no contribution to the surface integral

$$\int_S \mathrm{d}S\cos\left(\frac{N\pi}{L}y\right)(\bar{\rho}u' + \rho'\bar{u})_{n^-}^{n^+} = 0 \tag{22}$$

It is to be noted that the $\cos(N\pi y/L)$ factor in the preceding integral enables us to use the orthonormality property to reduce the preceding integration to an algebraic equation in the unknown coefficients.

2. *Linearized Momentum Equation*

The linearized momentum equation is given by

$$\frac{\partial(\bar{\rho}\mathbf{u}' + \rho'\bar{\mathbf{u}})}{\partial t} + \nabla\bullet(\bar{\rho}\,\bar{\mathbf{u}}\,\mathbf{u}' + \bar{\rho}\mathbf{u}'\bar{\mathbf{u}} + \rho'\bar{\mathbf{u}}\,\bar{\mathbf{u}} + p') = 0 \tag{23}$$

Multiplying the preceding equation with $\cos(N\pi y/L)$ and integrating over a differential volume of thickness dn across the interface, we get

$$\int_S \mathrm{d}S\cos\left(\frac{N\pi}{L}y\right)(2\bar{\rho}\,\bar{u}\,u' + \rho'\bar{u}\,\bar{u} + p')_{n^-}^{n^+} = 0 \tag{24}$$

3. *Linearized Energy Equation*

Neglecting kinetic energy and heat-release effects, the linearized energy equation can be written as

$$\frac{\partial(\bar{\rho}e' + \rho'\bar{e})}{\partial t} + \frac{\gamma}{\gamma-1}\nabla\bullet(\bar{\mathbf{u}}p' + \mathbf{u}'\bar{p}) = 0 \tag{25}$$

Using the same preceding procedure, we get

$$\int_S \mathrm{d}S\cos\left(\frac{N\pi}{L}y\right)(\bar{u}p' + u'\bar{p})_{n^-}^{n^+} = 0 \tag{26}$$

The preceding matching condition is, obviously, not valid at a flame surface. We now move on to apply the preceding zonal matching condition approach to the specific zonal interfaces α and β and the flame matching conditions.

G. Continuity Matching Conditions at the α Interface

The α interface occurs between zone 1 on the upstream side and zones 2 and 3 on the downstream side. At this interface, due to the change in cross section from zone 1 to zones 2 and 3, orthonormality can only be used in one of the three zones. We choose to use this property in zone 1 and hence multiply both sides of the continuity matching equation (refer Eq. (22)) with the factor:

$$\cos\left[\frac{N\pi}{\left(\frac{a-c}{2}\right)}\left(y - \frac{a+c}{2}\right)\right]$$

Upon simplification, we get the following equation:

$$\int_0^a \mathrm{d}y\cos\left[\frac{N\pi}{\left(\frac{a-c}{2}\right)}\left(y - \frac{a+c}{2}\right)\right](\bar{\rho}u' + \rho'\bar{u})_2 + \int_c^b \mathrm{d}y\cos\left[\frac{N\pi}{\left(\frac{a-c}{2}\right)}\left(y - \frac{a+c}{2}\right)\right](\bar{\rho}u' + \rho'\bar{u})_3 - \int_c^a \mathrm{d}y\cos\left[\frac{N\pi}{\left(\frac{a-c}{2}\right)}\left(y - \frac{a+c}{2}\right)\right](\bar{\rho}u' + \rho'\bar{u})_1 = 0 \tag{27}$$

Next, we substitute the respective zonal expressions for u' and ρ' into the preceding equation and apply orthonormality in zone 1 (third term on the left-hand side of the preceding equation). Orthonormality reduces the third integral to just one term, whereas the remaining two integrals, corresponding to zones 2 and 3, will each have two algebraic terms. One term will correspond to $n = N$ and the other $n \neq N$. The end result will be an algebraic equation corresponding to the continuity matching condition at the α interface. The details of this derivation are quite involved and laborious and are skipped here.

Similar matching conditions can be derived for momentum and energy equations at the α interface and are not included here in the interest of brevity.

H. Continuity Matching Conditions at the β Interface

At the β interface, we have separate matching conditions for the interfaces between zones 2 and 4 and zones 3 and 6. Next, we simply provide the continuity matching equations and leave out details of the corresponding momentum and energy equations.

For the interface between zones 2 and 4,

$$\int_0^a \mathrm{d}y \cos\left[\frac{N\pi}{(\frac{a}{2})}\left(y-\frac{a}{2}\right)\right](\bar{\rho}u'+\rho'\bar{u})_4 - \int_0^a \mathrm{d}y \cos\left[\frac{N\pi}{(\frac{a-c}{2})}\left(y-\frac{a}{2}\right)\right](\bar{\rho}u'+\rho'\bar{u})_2 = 0 \tag{28}$$

For the interface between zones 3 and 6,

$$\int_0^a \mathrm{d}y \cos\left[\frac{N\pi}{(\frac{b-c}{2})}\left(y-\frac{b+c}{2}\right)\right](\bar{\rho}u'+\rho'\bar{u})_6 - \int_0^a \mathrm{d}y \cos\left[\frac{N\pi}{(\frac{b-c}{2})}\left(y-\frac{b+c}{2}\right)\right](\bar{\rho}u'+\rho'\bar{u})_3 = 0 \tag{29}$$

The preceding equations are simplified into algebraic equations after a number of manipulations identical to the process described for continuity at the α interface.

I. Flame Matching Conditions

When applying matching conditions across the flame, we integrate the governing equations in a differential distance dn normal to the flame. The resultant linearized forms of the continuity, momentum, and energy matching conditions are presented next.

1. *Flame Continuity Matching Condition*

$$(\bar{\rho}u_n'+\rho'\bar{u}_n)|_{n^-}^{n^+}=0 \tag{30}$$

where subscript n refers to the vector component along the normal vector to the flame.

2. *Momentum Matching Condition Normal to the Flame*

$$(2\bar{\rho}\bar{u}_n u_n'+\rho'\bar{u}_n\bar{u}_n+p')|_{n^-}^{n^+}=0 \tag{31}$$

Assuming $\bar{u}_n/\bar{c} \ll 1$, we can write the linearized normal momentum-balance equation as

$$(p')|_{n^-}^{n^+}=0 \tag{32}$$

3. *Flame Energy Matching Condition*

The linearized energy equation here has an unsteady heat-release term, as shown next:

$$\frac{\partial(\bar{\rho}e'+\rho'\bar{e})}{\partial t}+\frac{\gamma}{\gamma-1}\nabla\bullet(\bar{u}p'+u'\bar{p})=q_v' \tag{33}$$

from which we get

$$(\bar{u}_n p'+u_n'\bar{p})|_{n^-}^{n^+}=\frac{\gamma-1}{\gamma}Q'_{\text{flame}} \tag{34}$$

where Q'_{flame} represents oscillations in the heat release per unit surface area of the flame.

Equations (30), (32), and (34) are applied across zones 4 and 5 and zones 5 and 6, giving rise to additional algebraic equations that form part of the larger system of equations to be solved for the unknown coefficients. Note that Q'_{flame} is not an inhomogeneous term, as heat-release fluctuations are ultimately expressed in terms of velocity fluctuations through the flame-response function and then combined with the terms on the left-hand side of Eq. (34). We will now demonstrate the functional form of the flame-normal fluctuating velocity u_n' that arises in Eq. (34).

4. *Functional Form of u_n'*

The flame-normal fluctuating velocity will be expressed in terms of the local streamwise and transverse velocity fluctuations u' and v' and the local flame-normal vector $\hat{\mathbf{n}}$. Let us first determine $\hat{\mathbf{n}}$. We know that

$$\hat{\mathbf{n}}=\frac{\nabla\bar{F}}{|\nabla\bar{F}|} \tag{35}$$

where $\bar{F}(x,y)=x-\bar{f}(y)=0$ is the mean flame-shape equation. This gives us

$$\hat{\mathbf{n}}=\frac{1}{\sqrt{1+(\frac{\partial\bar{f}}{\partial y})^2}}\hat{\mathbf{i}}-\frac{\frac{\partial\bar{f}}{\partial y}}{\sqrt{1+(\frac{\partial\bar{f}}{\partial y})^2}}\hat{\mathbf{j}} \tag{36}$$

where $\hat{\mathbf{i}}$ and $\hat{\mathbf{j}}$ are unit vectors in the x and y directions, respectively. We can then write u_n' as follows:

$$u_n'=(u'\hat{\mathbf{i}}+v'\hat{\mathbf{j}})\bullet\hat{\mathbf{n}}=\frac{1}{\sqrt{1+(\frac{\partial\bar{f}}{\partial y})^2}}u'-\frac{\frac{\partial\bar{f}}{\partial y}}{\sqrt{1+(\frac{\partial\bar{f}}{\partial y})^2}}v' \tag{37}$$

The mean flame shape $\bar{F}(x,y)$ is obtained from 2-D LES runs, as already indicated.

J. Inlet and Exit Boundary Conditions

1. *Inlet Impedance Boundary Condition*

The inlet boundary condition is usually specified in terms of known impedance Z_{inlet}. In the current study, Z_{inlet} was obtained from the 2-D LES study by averaging the impedance, defined as p'/u', across the inlet. We have

$$Z_{\text{inlet}}=\left.\frac{p'}{u'}\right|_{x=d} \tag{38}$$

Multiplying both sides of the preceding equation with

$$\cos\left[\frac{N\pi}{(\frac{a-c}{2})}\left(y-\frac{a+c}{2}\right)\right]$$

and integrating across the inlet cross section at $x=d$, we get

$$\int_c^a \mathrm{d}y \cos\left[\frac{N\pi}{(\frac{a-c}{2})}\left(y-\frac{a+c}{2}\right)\right]p'|_{x=d} = Z_{\text{inlet}}\int_c^a \mathrm{d}y \cos\left[\frac{N\pi}{(\frac{a-c}{2})}\left(y-\frac{a+c}{2}\right)\right]u'|_{x=d} \tag{39}$$

Using orthonormality, as before, the preceding equation can be reduced to an algebraic equation in the perturbation coefficients.

2. *Exit Boundary Condition*

For a choked nozzle exit, we have the following equation:

$$\left.\left(\frac{2u'}{\bar{u}}+\frac{\rho'}{\bar{\rho}}-\frac{p'}{\bar{p}}\right)\right|_{x=f}=0 \tag{40}$$

which gives a linear algebraic equation using the procedure outlined for the inlet boundary condition.

K. Equation Assembly and Solution

Upon substantial algebraic manipulation and assembly of the various equations, along with the boundary and matching conditions discussed earlier, we arrive at a homogeneous matrix system of the form

$$\mathbf{CA} = 0 \tag{41}$$

where $\mathbf{C}$ is the coefficient matrix and $\mathbf{A}$ is the variable vector consisting of the modal amplitudes in the various zones: $(A_n^{\pm})$, $(B_n^{\pm})$, and $(\hat{V}_n)$. Because the preceding matrix equation represents a system of homogeneous linear equations, a unique nontrivial solution exists only when $\det(\mathbf{C}) = 0$, which allows us to compute the complex eigenmodes $\Omega = \Omega_{\text{real}} + i\Omega_{\text{imag}}$. The real and imaginary parts of Ω correspond to the frequency and growth/decay rates of the combustor mode. Because the temporal functionality of the perturbations is represented by $e^{i\Omega t}$, it is clear that unstable modes Ω that grow in time have a negative imaginary part. Thus, a linear analysis will only provide the unstable modal shapes and frequencies and is silent on the limit-cycle behavior of the unstable modes. To investigate the limit-cycle behavior, one has to rely on nonlinear stability analysis.

Next, we present details of the G-equation approach used to derive the flame-response function that relates Q'_{flame} to flame-surface-area oscillations.

III. Flame-Response Model

The energy matching condition across the flame, given by Eq. (34), contains the heat-release term Q'_{flame} representing oscillations in heat release per unit surface area of the flame. A flame-response model is needed to compute Q'_{flame} as a function of the flame-surface-area fluctuations that in turn are a function of upstream velocity and vorticity fluctuations. The geometry of interest is illustrated schematically in Fig. 2. The duct height is taken to be $D = (a - c)$ and the flame is assumed to have a mean spatial extent f along the axial direction.

A. Basic Formulation

The instantaneous heat release per unit time from a differential element of area $\mathrm{d}A_{\text{in}}$ along the flame front is given by

$$\tilde{Q}(t, y) = \rho \tilde{s}_L \tilde{h}_r \, \mathrm{d}\tilde{A}_{\text{in}} \tag{42}$$

Introducing a turbulent flame speed s_T in the preceding equation, the ensemble-averaged heat release $Q(t, y)$ can be expressed as

$$Q(t, y) = \rho s_T h_r \, \mathrm{d}A \tag{43}$$

where $\mathrm{d}A$ is now the area element on the mean flame surface defined by the turbulent flame speed s_T. Splitting each term on the right-hand side of the preceding equation into time-mean and time-fluctuation components, we get

$$q(t, y) = \frac{Q(t, y)}{\mathrm{d}\bar{A}} = (\rho \bar{s}_T \bar{h}_r)\left[\left(1 + \frac{s'_T}{\bar{s}_T} + \frac{h'_r}{\bar{h}_r} + \frac{s'_L h'_r}{\bar{s}_L \bar{h}_r}\right) + \left(1 + \frac{s'_T}{\bar{s}_T} + \frac{h'_r}{\bar{h}_r} + \frac{s'_T h'_r}{\bar{s}_T \bar{h}_r}\right)\frac{\mathrm{d}A'}{\mathrm{d}\bar{A}}\right] \tag{44}$$

Time-averaging the preceding expression gives

$$\bar{q}(y) = (\rho \bar{s}_T \bar{h}_r)\left(1 + \frac{\overline{s'_T h'_r}}{\bar{s}_T \bar{h}_r} + \frac{\overline{s'_T \, \mathrm{d}A'}}{\bar{s}_T \, \mathrm{d}\bar{A}_r} + \frac{\overline{h'_r \, \mathrm{d}A'}}{\bar{h}_r \, \mathrm{d}\bar{A}} + \frac{\overline{s'_T h'_r \, \mathrm{d}A'}}{\bar{s}_T \bar{h}_r \, \mathrm{d}\bar{A}}\right) \tag{45}$$

Subtracting Eq. (45) from Eq. (44), we obtain the equation for the fluctuations in $q(t, y)$:

$$q'(t, y) = (\rho \bar{s}_T \bar{h}_r)\left(\frac{s'_T}{\bar{s}_T} + \frac{h'_r}{\bar{h}_r} + \frac{\mathrm{d}A'}{\mathrm{d}\bar{A}} + q'_{sA} + q'_{sh} + q'_{hA} + q'_{shA}\right) \tag{46}$$

where the nonlinear terms are

$$q'_{sA} = \frac{s'_T \, \mathrm{d}A' - \overline{s'_T \, \mathrm{d}A'}}{\bar{s}_T \, \mathrm{d}\bar{A}}, \qquad q'_{sh} = \frac{s'_T h'_r - \overline{s'_T h'_r}}{\bar{s}_T \bar{h}_r}$$
$$q'_{hA} = \frac{h'_r \, \mathrm{d}A' - \overline{h'_r \, \mathrm{d}A'}}{\bar{h}_r \, \mathrm{d}\bar{A}}, \qquad q'_{shA} = \frac{s'_T h'_r \, \mathrm{d}A' - \overline{s'_T h'_r \, \mathrm{d}A'}}{\bar{s}_T \bar{h}_r \, \mathrm{d}\bar{A}} \tag{47}$$

Thus, the ensemble-averaged heat-release ratio per unit area is given by

$$\frac{q'(t, y)}{\bar{q}(y)} = \left(\frac{s'_T}{\bar{s}_T} + \frac{h'_r}{\bar{h}_r} + \frac{\mathrm{d}A'}{\mathrm{d}\bar{A}} + q'_{sA} + q'_{sh} + q'_{hA} + q'_{shA}\right), \qquad \bar{q}(y) = \rho \bar{s}_T \bar{h}_r \tag{48}$$

B. Linearized Heat-Release Model

Retaining terms that are first order in fluctuating quantities,

$$\frac{q'(t, y)}{\bar{q}(y)} = \frac{s'_T}{\bar{s}_T} + \frac{h'_r}{\bar{h}_r} + \frac{\mathrm{d}A'}{\mathrm{d}\bar{A}} \tag{49}$$

Taking the Fourier transform with respect to time, we get

$$\frac{\hat{q}'(\Omega, y)}{\bar{q}(y)} = \frac{\hat{s}'_T}{\bar{s}_T} + \frac{\hat{h}'_r}{\bar{h}_r} + \frac{\mathrm{d}\hat{A}'}{\mathrm{d}\bar{A}} \tag{50}$$

Note that the linearized perturbations are coherent in nature (i.e., different from the stochastic turbulent fluctuations) and are imposed on ensemble- and time-averaged conditions of the system. Assuming a premixed flame (i.e., no perturbations in the equivalence ratio), the first two terms on the right-hand side of Eq. (50) can be neglected (see Fig. 3). Hence, we retain only the flame-surface-area fluctuation term $\mathrm{d}\hat{A}'/\mathrm{d}\bar{A}$, which is a result of the coherent perturbations superimposed on the mean flow conditions. We assume that the mean flame shape and the perturbed flame shape (due to coherent perturbations) are simply connected and single-valued. This assumption is valid because we are only interested in the stability of the mean system conditions when subjected to low-amplitude (compared with the mean) perturbations.

From Eq. (50), it is required to determine the flame-surface-area fluctuation at the forcing frequency. The coherent component of the flame-surface oscillation (i.e., $\mathrm{d}\hat{A}'/\mathrm{d}\bar{A}$) at any time is governed in the corrugated flamelet regime by the following the G-equation:

$$\frac{\partial G}{\partial t} + \mathbf{v} \bullet \nabla G = s_T |\nabla G| \tag{51}$$

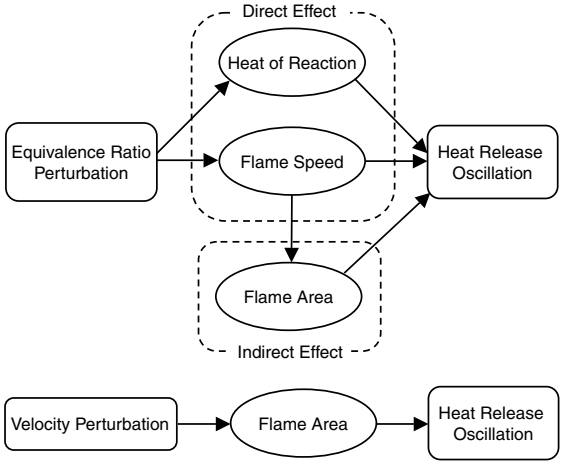

Fig. 3 Fundamental processes causing heat-release oscillation due to equivalence ratio and velocity perturbations (in the current analysis, only velocity perturbations give rise to heat-release oscillations).

It is assumed that the coherent flame surface is simply connected and single-valued. As such, this leads to the choice of $G(x, y, t) = x - f(y, t)$, where $f(y, t)$ is shown schematically in Fig. 2. Using this expression for G in Eq. (51), we have

$$f_t - u + vf_y = -s_T\sqrt{1 + f_y^2} \tag{52}$$

where subscripts denote differentiation. Separating the preceding into a steady mean component and a fluctuating component and linearizing, we obtain

$$f_t' - \bar{u} + \bar{v}\bar{f}_y - u' + v'\bar{f}_y + \bar{v}f_y' = -\bar{s}_T\sqrt{1 + \bar{f}_y^2} - \frac{\bar{s}_T\bar{f}_y}{\sqrt{1 + \bar{f}_y^2}}f_y' - s_T'\sqrt{1 + \bar{f}_y^2} \tag{53}$$

Splitting the preceding equation into two equations for the time-mean and time-fluctuating components, we obtain

$$\bar{u} - \bar{v}\bar{f}_y = \bar{s}_T\sqrt{1 + \bar{f}_y^2} \tag{54}$$

$$f_t' + g(y)f_y' = (u_n' - s_T')\sqrt{1 + \bar{f}_y^2} \tag{55}$$

where

$$g(y) = \frac{\bar{s}_T\bar{f}_y}{\sqrt{1 + \bar{f}_y^2}} + \bar{v}, \qquad u_n'(y) = \frac{u' - v'\bar{f}_y}{\sqrt{1 + \bar{f}_y^2}} \tag{56}$$

Assuming harmonic temporal variations for fluctuating quantities (e.g., $f'(y, t) = \hat{f}'(y)e^{i\Omega t}$), we have

$$\frac{\mathrm{d}\hat{f}'}{\mathrm{d}y} + \frac{i\Omega}{g(y)}\hat{f}' = \frac{(\hat{u}_n' - \hat{s}_T')}{g(y)}\sqrt{1 + \bar{f}_y^2} \tag{57}$$

The preceding equation is then made dimensionless using

$$\hat{F} = \hat{f}/L_f, \qquad \bar{y} = y/a, \qquad \hat{u}_n^* = \hat{u}_n/\bar{u}, \qquad \beta = L_f/a \tag{58}$$

Thus, we have for the flame-surface shape,

$$\frac{\mathrm{d}\hat{F}}{\mathrm{d}\bar{y}} + \frac{i(St)}{\beta\bar{g}(\bar{y})}\hat{F} = \frac{(\hat{u}_n^* - \hat{s}_T^*)}{\beta\bar{g}(\bar{y})}\sqrt{1 + (\beta\bar{F}_{\bar{y}})^2} \tag{59}$$

where

$$St = \frac{\Omega L_f}{\bar{u}}, \qquad \bar{g}(\bar{y}) = \frac{\bar{s}_T\beta\bar{F}_{\bar{y}}}{\bar{u}\sqrt{1 + (\beta\bar{F}_{\bar{y}})^2}} + \frac{\bar{v}}{\bar{u}} \tag{60}$$

We now use the boundary condition that the flame stays attached to the bluff body at all times. Integrating Eq. (59) using the boundary condition yields

$$\hat{F}(\bar{y}) = \int_0^{\bar{y}} \exp\left(i(St)\int_{\bar{y}}^{\eta}\frac{\mathrm{d}\rho}{\beta\bar{g}(\rho)}\right)\left\{\frac{[\hat{u}_n^*(\eta) - \hat{s}_T^*(\eta)]}{\beta\bar{g}(\eta)}\sqrt{1 + (\beta\bar{F}_{\bar{y}})^2}\right\}\mathrm{d}\eta \tag{61}$$

Now consider an area element on the flame surface. We have

$$\mathrm{d}A = \sqrt{(\mathrm{d}x)^2 + (\mathrm{d}y)^2} = \mathrm{d}y\sqrt{1 + \left(\frac{\mathrm{d}f}{\mathrm{d}y}\right)^2} \tag{62}$$

Decomposing $\mathrm{d}A$ into mean and fluctuating quantities, we get the following expression for the area ratio $\mathrm{d}\hat{A}'/\mathrm{d}\bar{A}$:

$$\frac{\mathrm{d}\hat{A}'}{\mathrm{d}\bar{A}} = \left(\frac{\bar{f}_y}{1 + \bar{f}_y^2}\hat{f}_y'\right) = \left(\frac{\beta^2\bar{F}_{\bar{y}}}{1 + (\beta\bar{F}_{\bar{y}})^2}\right)\hat{F}_{\bar{y}} \tag{63}$$

Differentiating Eq. (61) with respect to $\bar{y}$, we have

$$\hat{F}_{\bar{y}}(\bar{y}) = \frac{(\hat{u}_n^*(\bar{y}) - \hat{s}_T^*(\bar{y}))}{\beta\bar{g}(\bar{y})}\sqrt{1 + (\beta\bar{F}_{\bar{y}})^2} + i(St)\int_0^{\bar{y}}\exp\left(i(St)\int_{\bar{y}}^{\eta}\frac{\mathrm{d}\rho}{\beta\bar{g}(\rho)}\right) \times \left\{\frac{(\hat{s}_T^*(\eta) - \hat{u}_n^*(\eta))}{(\beta\bar{g}(\eta))^2}\sqrt{1 + (\beta\bar{F}_{\bar{y}})^2}\right\}\mathrm{d}\eta \tag{64}$$

Using the preceding in Eq. (63) yields the desired result:

$$\frac{Q'_{\mathrm{flame}}}{\bar{q}} = \frac{q'}{\bar{q}} = \frac{\mathrm{d}\hat{A}'}{\mathrm{d}\bar{A}} = \frac{\beta\bar{F}_{\bar{y}}}{\sqrt{1 + (\beta\bar{F}_{\bar{y}})^2}}\frac{(\hat{u}_n^*(\bar{y}) - \hat{s}_T^*(\bar{y}))}{\bar{g}(\bar{y})} + \frac{i(St)\bar{F}_{\bar{y}}}{\{1 + (\beta\bar{F}_{\bar{y}})^2\}|_{\bar{y}}}\int_0^{\bar{y}}\exp\left(i(St)\int_{\bar{y}}^{\eta}\frac{\mathrm{d}\rho}{\beta\bar{g}(\rho)}\right) \times \left\{\frac{[\hat{s}_T^*(\eta) - \hat{u}_n^*(\eta)]}{[\bar{g}(\eta)]^2}\sqrt{1 + (\beta\bar{F}_{\bar{y}})^2}\right\}\mathrm{d}\eta \tag{65}$$

The preceding equation relates flame heat-release fluctuations per unit surface to those in the flame-surface area. We can input any mean flame shape of interest into the preceding equation and obtain the appropriate expression for the heat-release fluctuation rate. The mean flame shape $\bar{F}_{\bar{y}}$ and the mean heat-release rate $\bar{q}$ are both obtained from the 2-D LES simulations.

The preceding expression for $Q'_{\mathrm{flame}}/\bar{q}$ completes the reduced-order model developed in the previous sections. We now proceed to discuss the application of the total model to a bluff-body-stabilized flame and compare model predictions with 2-D LES results, when available.

IV. Results and Model Validation

For testing the reduced-order model in conjunction with the flame-response function, a simplified single-element flameholder was analyzed, as shown in Fig. 2. Five test cases with varying geometries (i.e., duct length and height), flameholder locations (with and without vertical offset), and mean flame shapes were considered. Two of the cases had resolved-LES data to compare with. We begin with a discussion of the results obtained from the 2-D LES study. Subsequently, a discussion of the various test cases and of the unstable-frequency predictions obtained using the reduced-order model are presented.

A. Two-Dimensional LES Study

The commercial CFD code CFD-ACE+, originally developed at CFD Research Corporation, has been used to perform the LES study. CFD-ACE+ is a highly validated code that has been used both in government laboratories and in industry for more than a decade now. The localized dynamic subgrid-kinetic-energy model [36] was used to compute subgrid-scale stresses in the filtered Navier–Stokes equations.

Two highly resolved 2-D LES runs of a premixed propane–air-mixture flow over a bluff body were performed. Near-wall grid resolution employed was sufficiently fine for the purposes of resolved LES, with $y^+ \sim 1$. In the first case, the bluff body was located symmetrically between the two transverse (y direction) boundaries of the domain, whereas in the second case, the bluff body was 0.1 in. closer to the top wall than to the bottom wall. Freestream conditions for both LES runs are identical and are indicated in Table 1, and the LES flameholder geometry is given in Fig. 4. Mean flow data from the two LES runs serve as inputs to the reduced-order model.

Mean temperature contours for the two cases are shown in Fig. 5. In Fig. 5a, in which the bluff body is located symmetrically between

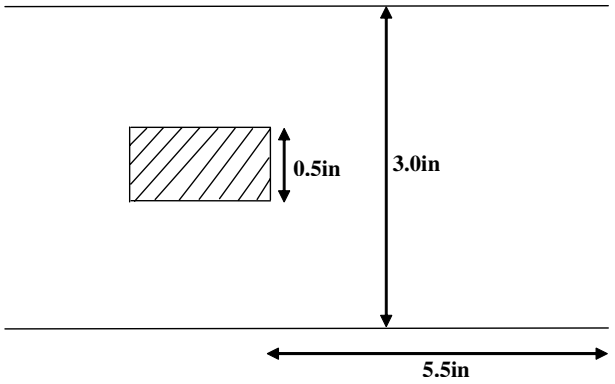

Fig. 4 Schematic of bluff-body flameholder geometry for 2-D LES (flow is from left to right).

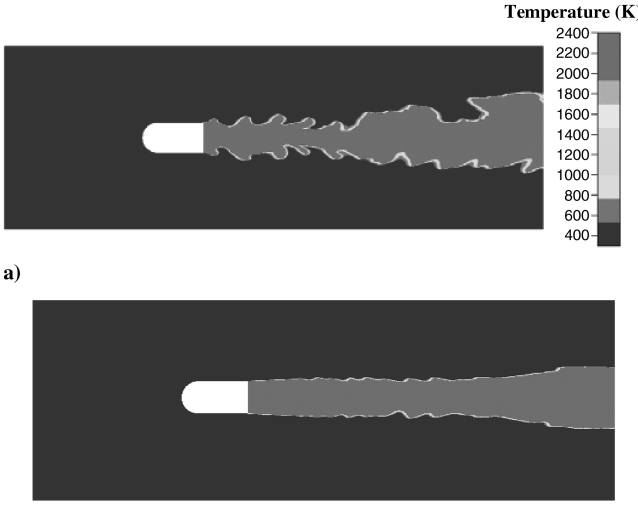

Fig. 5 Two-dimensional LES temperature contours with a) no vertical offset and b) a 0.1 in. vertical offset.

the two y-direction boundaries, we can clearly observe the flame-surface instabilities. From Fig. 5b, it is clear that a small vertical offset of 0.1 in. toward the top wall damps out the instabilities observed without the vertical offset. This fact is further elucidated by the frequency spectra of pressure for the two cases, which are presented in the next subsection.

B. Reduced-Order-Model Results

1. *Case 1 (Baseline Case)*

The flow and geometrical parameters for this case are obtained from 2-D LES and are presented in Table 1. The main geometrical feature of this case is that the *bluff body is located symmetrically between the top and bottom walls of the duct*: that is, the bluff body has no vertical offset.

Previous 2-D reacting-flow LES calculations of this baseline case predicted a transverse instability (see Fig. 5a). Thus, this case

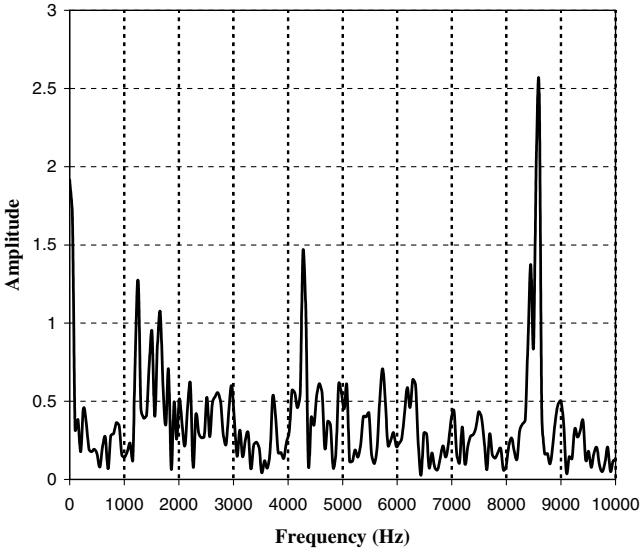

Fig. 6 Pressure oscillation amplitude vs frequency data obtained from 2-D LES with no vertical offset of the bluff body.

provided a good test case for the reduced-order analysis. The mean flame shape in the 2-D LES study was obtained by ensemble-averaging over a large number of temporal snapshots of the flame. The flame-shape temporal snapshots were collected over a number of flow-through times (time taken by the mean flow from the inlet of the domain to the exit) after the LES had reached a statistically stationary state. The spatial (x, y) coordinates of the mean flame shape were then extracted and provided as input to the reduced-order model.

Shown in Fig. 6 is a plot of the amplitude of pressure oscillations vs frequency ($\Omega_{\text{real}}/2\pi$ according to our notation) obtained by a Fourier transform of 2-D LES time-series data into the frequency domain. Three dominant frequencies (at approximately 1200, 4400, and 8600 Hz) are clearly seen in Fig. 6. These frequencies are believed to correspond to a fundamental axial mode (1200 Hz) and a fundamental transverse mode (4400 Hz) and its harmonic (8600 Hz).

The baseline case was run through the reduced-order analysis code, and the unstable-frequency predictions and growth rates obtained are compared with LES predictions in Table 2. Reasonably good agreement between the LES and reduced-order model predictions is seen. Also presented in Table 2 are unstable frequencies that are captured by the reduced-order model, but not observed as large amplitude oscillations in the LES data. These additional unstable modes are probably harmonics of fundamental modes that have been damped out in the LES analysis.

Simple acoustic analysis shows that the 4556 Hz frequency is determined by the height of the duct, whereas the 1200 Hz mode is most probably determined by the axial length of the duct downstream of the flameholder. We can also see that qualitatively the fastest initial growth rate seen for the 8912 Hz corresponds to the maximum amplitude seen in Fig. 6 for this mode. Further, the axial harmonics 2414 and 3731 Hz have the slowest initial growth rates, which is in qualitative agreement with the lower amplitudes seen for these frequencies in Fig. 6.

Table 2 Comparison of LES and model predictions for case 1

LES frequency, Hz	Model-predicted unstable frequency, Hz	Growth-rate parameter Ω_{imag}	Probable mode type
1200	1306	−20.3	Axial (fundamental)
——	2414	−12.2	Axial (first harmonic)
——	3731	−18.6	Axial (second harmonic)
4400	4556	−33.6	Transverse (fundamental)
8600	8912	−46.2	Transverse (first harmonic)

Table 3 Effect of duct height increase on unstable modes

Model-predicted unstable frequency, Hz	Growth-rate parameter Ω_{imag}	Probable mode type
1354	−16.7	Axial (fundamental)
1880	−36.2	Mixed mode
3244	−20.6	Transverse (fundamental)
4114	−19.4	Axial (second harmonic)
6886	−38.3	Transverse (first harmonic)
9356	−41.2	Transverse (second harmonic)

Table 4 Effect of duct length increase on unstable modes

Model-predicted unstable frequency, Hz	Growth-rate parameter Ω_{imag}	Probable mode type
856	−33.8	Axial (fundamental)
1346	−31.4	Axial (first harmonic)
4443	−26.4	Transverse (fundamental)
8712	−42.3	Transverse (first harmonic)

2. Case 2

All flow conditions and geometry for this case are same as those for the baseline case, except for the duct height, which is 1.5 times the duct height of the baseline case (4.5 vs 3.0 in.). The flameholder is located symmetrically between the two duct walls. This case was chosen to determine the effects of duct height on unstable modes predicted by the reduced-order model. However, there are no LES results to compare with for this case. Unstable frequency predictions and their growth rates are shown in Table 3. The predicted fundamental transverse frequency (3244 Hz) correctly reflects the effect of increased duct height on the unstable-frequency magnitudes, i.e., increase in duct height leads to a reduction in the fundamental transverse frequency and its harmonics. The fundamental axial mode, however, does not change significantly, which is to be expected because the duct length is the same as in case 1.

3. Case 3

This case is same as the baseline except for the duct length downstream of the bluff body (f in Fig. 2), which is twice that of the baseline case (11.0 vs 5.5 in.). There are no LES data for this case as well. The predicted axial fundamental frequency is 856 Hz for this case (see Table 4), which is to be expected because of the increased duct length. The transverse unstable frequencies did not change significantly compared with the baseline case, also as expected.

4. Case 4

The flow parameters in case 4 are identical to those in case 1. The flame shape, however, differs from that in Fig. 2. The new flame configuration is shown in Fig. 7. This time, the flame touches the wall at $x = f$. There is, however, no LES data for this case. The purpose of this case was to investigate combustion instability when the flame touches the walls.

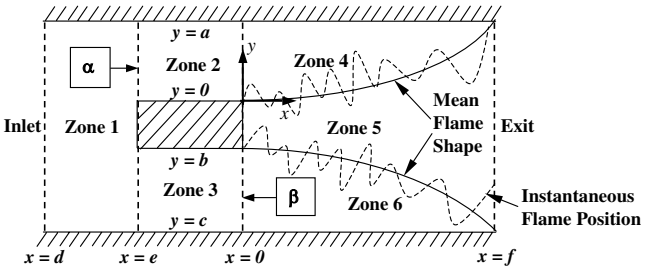

Fig. 7 Flame configuration for case 4 with the flame touching the top and bottom walls.

Table 5 Unstable frequency data obtained from the reduced-order model for case 4

Model frequency, Hz	Growth-rate parameter Ω_{imag}	Probable mode type
1389	−18.1	Axial (fundamental)
1870	−9.3	Mixed
4810	−26.3	Transverse (fundamental)
9245	−32.5	Transverse (first harmonic)

Unstable mode frequencies for case 4, obtained from the reduced-order model, are tabulated in Table 5. It is observed that there is an increase in the values of unstable transverse frequencies from 4556 Hz in case 1 to 4810 Hz in case 4, and from 8912 Hz in case 1 to 9245 Hz in case 4. On the other hand, the growth rates of these modes when the flame touches the walls are lower than when the flame does not touch the walls (case 1). Thus, the reduced-order model predicts that the flame-wall interaction results in smaller initial growth rates of the linearly unstable modes.

5. Case 5

The flow and geometrical parameters for this case are identical to those for case 1, *but the bluff body is offset vertically toward the upper wall by* 0.1 in. The 2-D LES study for this case shows low-amplitude pressure oscillations across the entire frequency range (see Fig. 8).

Model predictions for the offset and the zero-offset flameholder configurations are presented in Table 6. The reduced-order model predicts essentially the same unstable frequencies for the offset case as the zero-offset baseline case. However, the initial growth rates of unstable frequencies for the offset case are lower than those for the baseline case. Whether this translates into the LES-observed lower limit-cycle amplitudes for the offset case is open to conjecture. A nonlinear analysis will be required to determine these limit-cycle pressure amplitudes.

V. Conclusions

Detailed derivation of a 2-D reduced-order model and the flame-response function for a flameholder-stabilized flame of arbitrary mean shape was presented. Highly resolved 2-D LES simulations were performed for two configurations: without (case 1) and with (case 5) vertical offset of the bluff body. In the former configuration,

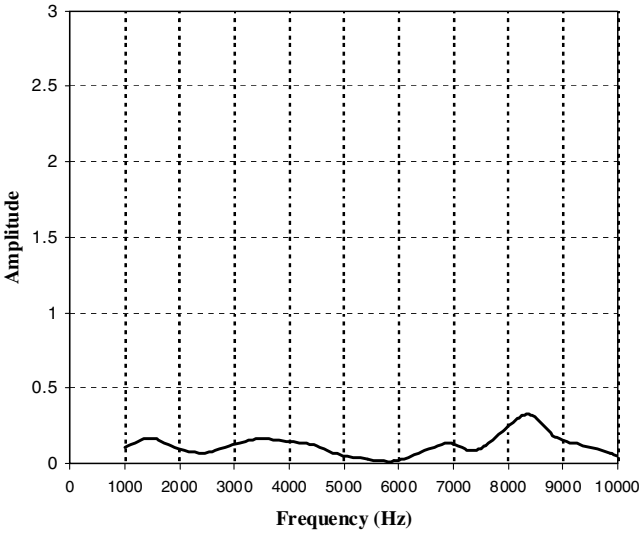

Fig. 8 Pressure oscillation amplitude vs frequency data obtained from 2-D LES with the bluff body offset vertically by 0.1 in.

Table 6 Comparison of LES and model predictions for case 5

Model-predicted unstable frequency with vertical offset, Hz	Growth-rate parameter Ω_{imag} with vertical offset	Model-predicted unstable frequency with zero offset (case 1), Hz	Growth-rate Ω_{imag} with zero offset (case 1)
1412	−17.9	1306	−20.3
4246	−29.6	4556	−33.6
8722	−42.1	8912	−46.2

LES predicts a dominant transverse mode, whereas in the latter, the small vertical offset is shown to damp out this mode. Good quantitative agreement was found between the model predictions and 2-D LES data for case 1. For case 5, the model predicts unstable frequencies with smaller growth rates than those of the corresponding unstable modes in case 1. But no information can be drawn regarding the limit-cycle behavior of the model-predicted unstable modes for case 5, and we can only say that the model shows qualitative agreement with LES. Variations in duct geometry also produced qualitatively consistent model unstable-frequency predictions.

Acknowledgments

This work was performed as part of a U.S. Air Force Phase I Small Business Innovation Research project funded by the U.S. Air Force Research Laboratory (Dayton, OH) under contract FA865006M2655. The author is grateful to Tim Lieuwen and Santosh Hemchandra of Georgia Institute of Technology for their help in deriving the flame-response model and for many useful discussions.

References

[1] Williams, G., Hottel, H., and Scurlock, A., "Flame Stabilization and Propagation in High Velocity Gas Streams," *Proceedings of the Combustion Institute*, Vol. 3, 1951, pp. 21–40.

[2] Longwell, J. P., Chenevey, J., Clark, W., and Frost, E., "Flame Stabilization by Baffles in a High Velocity Gas Stream," *Proceedings of the Combustion Institute*, Vol. 3, 1951, pp. 40–44.

[3] Williams, G. C., and Shipman, C. W., "Some Properties of Rod Stabilized Flames of Homogenized Gas Mixtures," *Proceedings of the Combustion Institute*, Vol. 4, 1953, pp. 733–742.

[4] Zukoski, E. E., and Marble, F. E., "The Role of Wake Transition in the Process of the flame Stabilization in Bluff Bodies," *AGARD Combustion Researches and Reviews*, Butterworth Scientific, London, 1955, pp. 167–180.

[5] Jensen, W. P., and Shipman, C. W., "Stabilization of the flames in High Speed Flows by Pilot Flames," *Proceedings of the Combustion Institute*, Vol. 7, 1958, pp. 674–680.

[6] Cheng, S. I., and Kovitz, A. A., "Theory of the flame Stabilization by a Bluff Body," *Proceedings of the Combustion Institute*, Vol. 7, 1958, pp. 681–691.

[7] Soteriou, M. C., and Mehta, P. G., "Combustion Heat Release Effects on the Dynamics of a Bluff Body Stabilized Premixed Reacting Flows," AIAA Paper 2003-0835, 2003.

[8] Straub, D. L., and Richards, G. A., "Effect of Fuel Nozzle Configuration on Premixed Combustion Dynamics," ASME Turbo Expo, Stockholm, Sweden, American Society of Mechanical Engineers Paper 1998-GT-492, 1998.

[9] Ducruix, S., Schuller, T., Durox, D., and Candel, S. M., "Combustion Dynamics and Instabilities: Elementary Coupling and Driving Mechanisms," *Journal of Propulsion and Power*, Vol. 19, No. 5, 2003, pp. 722–734. doi:10.2514/2.6182

[10] Lieuwen, T., "Modeling Premixed Combustion-Acoustic Wave Interactions: A Review," *Journal of Propulsion and Power*, Vol. 19, No. 5, 2003, pp. 765–781. doi:10.2514/2.6193

[11] Dowling, A. P., and Stow, S. R., "Acoustic Analysis of Gas Turbine Combustors," *Journal of Propulsion and Power*, Vol. 19, No. 5, 2003, pp. 751–764. doi:10.2514/2.6192

[12] Akamatsu, S., and Dowling, A. P., "Three Dimensional Thermoacoustic Oscillation in a Premix Combustor," ASME Turbo Expo, New Orleans, LA, American Society of Mechanical Engineers Paper 2001-GT-0034, 2001, June 4–7, 2001.

[13] Hubbard, S., and Dowling, A. P., "Acoustic Instabilities in Premix Burners," AIAA Paper 98-2272, 1998.

[14] Hubbard, S., and Dowling, A. P., "Acoustic Resonances of an Industrial Gas Turbine System," *Journal of Engineering for Gas Turbines and Power*, Vol. 123, No. 4, 2001, pp. 766–773. doi:10.1115/1.1370975

[15] Dowling, A. P., and Hubbard, S., "Instability in Lean Premixed Combustors," *Proceedings of the Institution of Mechanical Engineers Part A, Journal of Power Engineering*, Vol. 214, No. 4, 2000, pp. 317–332. doi:10.1243/0957650001537903

[16] Stow, S. R., and Dowling, A. P., "Thermoacoustic Oscillations in an Annular Combustor," ASME Turbo Expo, New Orleans, LA, American Society of Mechanical Engineers, Paper 2001-GT-0037, 2001.

[17] Armitage, C. A., Cant, R. S., Dowling, A. P., and Hynes, T. P., "Linearized Theory for LPP Combustion Dynamics," ASME Turbo Expo, Atlanta, American Society of Mechanical Engineers Paper 2003-GT-38670, 2003.

[18] Fleifil, M., Annaswamy, A. M., Ghoneim, Z. A., and Ghoniem, A. F., "Response of a Laminar Premixed Flame to Flow Oscillations: A Kinematic Model and Thermoacoustic Instability Results," *Combustion and Flame*, Vol. 106, No. 4, 1996, pp. 487–510. doi:10.1016/0010-2180(96)00049-1

[19] Wee, D., Park, S., Annaswamy, A. M., and Ghoniem, A. F., "Reduced Order Modeling of the Reacting Shear Flow," AIAA Paper 2002-0478, 2002.

[20] You, D., Yang, V., and Sun, X., "*Three-Dimensional Linear Stability Analysis of Gas Turbine Combustion Dynamics*," Combustion Instabilities in Gas Turbine Engines, Progress in Aeronautics and Astronautics, Vol. 210, edited by T. Lieuwen, and V. Yang, AIAA, Reston, VA, 2005, pp. 415–443.

[21] Culick, F. E. C., "Nonlinear Behavior of Acoustic Waves in Combustion Chambers—1," *Acta Astronautica*, Vol. 3, 1976, pp. 715–734. doi:10.1016/0094-5765(76)90107-7

[22] Culick, F. E. C., "Nonlinear Behavior of Acoustic Waves in Combustion Chambers—2," *Acta Astronautica*, Vol. 3, 1976, pp. 735–757. doi:10.1016/0094-5765(76)90108-9

[23] Culick, F. E. C., "Some Recent Results for Nonlinear Acoustics in Combustion Chambers," *AIAA Journal*, Vol. 32, No. 1, 1994, pp. 146–169. doi:10.2514/3.11962

[24] Bumley, V. S., and Culick, F. E. C., "Influence of Random Excitations on Acoustic Instabilities in Combustion Chambers," *AIAA Journal*, Vol. 38, No. 8, 2000, pp. 1403–1410. doi:10.2514/2.1116

[25] Margolis, S. B., "Nonlinear Stability of Combustion-Driven Acoustic Oscillations in Resonance Tubes," *Journal of Fluid Mechanics*, Vol. 253, 1993, pp. 67–104. doi:10.1017/S0022112093001727

[26] Margolis, S. B., "The Nonlinear Dynamics of Intrinsic Acoustic Oscillations in a Model Pulse Combustor," *Combustion and Flame*, Vol. 99, No. 2, 1994, pp. 311–322. doi:10.1016/0010-2180(94)90136-8

[27] Margolis, S. B., "Resonant Mode Interactions and the Bifurcation of Combustion-Driven Acoustic Oscillations in Resonance Tubes," *SIAM Journal on Applied Mathematics*, Vol. 54, No. 6, 1994b, pp. 1594–1633. doi:10.1137/S0036139993242558

[28] Flandro, G. A., Fischbach, S. R., Majdalani, J., and French, J. C., "Nonlinear Rocket Motor Stability Prediction: Limit Amplitude, Triggering, and Mean Pressure Shift," AIAA Paper 2004-4054.

[29] Lieuwen, T., "Investigation of Combustion Instability Mechanisms in

Premixed Gas Turbines," Ph.D. Thesis, Georgia Inst. of Technology, Atlanta, Aug. 1998.
[30] Lieuwen, T., and Neumeier, Y., "Nonlinear Pressure-Heat Release Transfer Function Measurements in a Premixed Combustor," *Proceedings of the Combustion Institute*, Vol. 29, No. 1, 2002, pp. 99–105. doi:10.1016/S1540-7489(02)80017-7
[31] Preetham, S. H., and Lieuwen, T. C., "Response of Turbulent Premixed Flames to Harmonic Acoustic Forcing," *Proceedings of the Combustion Institute*, Vol. 31, No. 1, 2007, pp. 1427–1434. doi:10.1016/j.proci.2006.07.198
[32] Preetham, Sai Kumar, T., and Lieuwen, T., "Response of Premixed Flames to Flow Oscillations: Unsteady Curvature Effects," AIAA Paper 2006-0960, 2006.
[33] Dowling, A. P., "A Kinematic Model of a Ducted Flame," *Journal of Fluid Mechanics*, Vol. 394, 1999, pp. 51–72. doi:10.1017/S0022112099005686
[34] Kopitz, J., Huber, A., Sattelmayer, T., and, Polifke, W., "Thermoacoustic Stability Analysis of an Annular Combustion Chamber with Acoustic Low Order Modeling and Validation against Experiment," ASME Turbo Expo, Reno-Tahoe, NV, American Society of Mechanical Engineers Paper GT2005-68797, 2005.
[35] Glassman, I., *Combustion*, Academic Press, New York, 3rd ed., 1996.
[36] Kim, W.-W., and Menon, S., "Application of the Localized Dynamic Subgrid-Scale Model to Turbulent Wall-Bounded Flows," 35th Aerospace Sciences Meeting and Exhibit, AIAA Paper 1997-0210, Reno, NV, 1997.

D. Talley
Associate Editor